POAC'25
St. John's, Newfoundland and Labrador, Canada

Proceedings of the 28th International Conference on Port and Ocean Engineering under Arctic Conditions
Jul 13-17, 2025
St. John's, Newfoundland and Labrador
Canada

Airflow Characterization of an NREL S809 Wind Turbine Blade with Particle Image Velocimetry

Ramnina Betsarkes, Kevin Pope, Yuri Muzychka
Department of Mechanical and Mechatronics Engineering
Memorial University of Newfoundland, Canada

ABSTRACT

This study presents new particle image velocimetry data on the airflow patterns over a wind turbine blade. An NREL S809 2D blade with a chord length of 0.3 m is tested in an open-return wind tunnel at Memorial University of Newfoundland. The effects of the angle of attack on the velocity field and boundary layer characteristics are investigated. These airflow patterns are analyzed to identify regions prone to droplet impingement, which affects ice accumulation on wind turbine blades. The results indicate that the airflow remains attached at a low angle of attack, leading to a symmetric wake and stable flow over the airfoil surface. However, at an angle of attack of 20°, flow separation occurs near the leading edge, resulting in high turbulence energy and strong vortex formation. This enhanced vortex structure may disperse droplets, potentially reducing ice accumulation on the blade. These findings provide valuable insights into improving wind turbine performance and developing effective ice mitigation strategies for cold-weather conditions.

KEY WORDS: Wind Turbine Blade, Particle Image Velocimetry, Wind Tunnel, Velocity Vector Fields, Turbulence Intensity.

INTRODUCTION

In cold northern regions, wind speeds are typically 10% higher than in other locations, and there is higher energy density due to more dense air (Parent and Ilinca, 2011). The power production capacity of wind turbines in Canada is projected to reach 23 GW by 2035 (Canada. National Energy Board 2023). Despite these advantages, cold climates present challenges, particularly ice formation on wind turbine blades.

Ice accumulation on wind turbine blades alters the aerodynamic properties of the airfoil by increasing surface roughness, leading to a rise in the drag coefficient and a decline in total energy output (Kelly et al., 2021). The irregular shapes of ice deposits create imbalanced mass distributions, resulting in uneven loading on the blades, which can cause structural vibrations and increase fatigue loads. In severe icing conditions, turbines must be shut down to prevent mechanical failure due to changes in their natural frequency, further reducing power production. The energy generation loss due to icing has been reported to be as high as 17% of the total annual energy production (Barber et al., 2011). In unusual cases, ice accretion can lead to excessive power generation, posing risks of overloading and shortening the lifespan of turbine components (Ibrahim et al., 2023). To overcome these challenges, understanding and mitigating the effects of icing are essential for optimizing wind turbine performance in cold environments.

The S809 airfoil, developed by the National Renewable Energy Laboratory (NREL), is widely used in wind turbine blade designs due to its high energy efficiency and relatively low sensitivity to surface roughness effects (Maldonado et al., 2015). Nonetheless, its aerodynamic performance in icing conditions remains an area of ongoing investigation. Advanced flow measurement techniques such as Particle Image Velocimetry (PIV) are broadly used to analyze airflow patterns and turbulence characteristics over airfoils to investigate the phenomena. PIV is a high-resolution optical technique that allows for the detailed visualization of velocity fields, providing critical insights into aerodynamic behavior under various operating conditions.

Previous studies have utilized PIV to examine the stall dynamics of the S809 airfoil, showing that at high Angles of Attack (AOA = 40°), a deep stall occurs, leading to vortex shedding at the trailing edge and full boundary layer separation on the pressure side of the airfoil (Ma et al., 2010). Additionally, studies have explored methods for improving aerodynamic performance, such as employing high-pressure jets in separated regions to reduce the extent of flow separation (Xie et al., 2013). Similarly, volumetric PIV systems have been implemented to investigate laminar separation bubbles on airfoils, analyzing Reynolds stresses to determine transition and reattachment regions (Wahidi et al., 2013). Increasing the turbulence intensity in the freestream has been found to delay flow separation, enhancing aerodynamic efficiency (Maldonado et al., 2015).

Understanding the airflow pattern over wind turbine blades is a key factor in designing icing mitigation systems. More specifically, at the point of impingement, the droplets will freeze under rime ice conditions. In this regard, studying airflow provides insight into the ice accumulation regions. Under these conditions, small supercooled droplets follow the airflow streamlines closely and have a broader impingement area due to their lower velocities (Wu et al., 2023). Aerodynamic features such as flow separation and velocity gradients directly influence the trajectory of droplets, affecting ice accumulation patterns. Li et al. (Li et al., 2019) demonstrated the significance of linking airflow patterns with droplet trajectories to characterize rime ice formation using PIV measurements. Additionally, icing severity varies depending on atmospheric conditions; for instance, the performance reduction due to ice accretion during the rime ice regime can range from 5 – 25%, while in glaze ice conditions, losses can exceed 70% (Han et al., 2012).

This paper investigates the airflow patterns over an S809 airfoil subjected to high turbulence intensity, replicating the wake effects of an upstream turbine at various angles of attack using particle image velocimetry. By analyzing the velocity distribution and wake development, the boundary layer characteristics are examined to identify regions susceptible to ice accumulation under rime ice conditions. The findings will contribute to the development of effective mitigation strategies to enhance wind turbine performance in cold environments.

EXPERIMENTAL SETUP

The experiments are conducted in an open-return wind tunnel at Memorial University of Newfoundland. The wind tunnel consists of three interconnected sections, each with a length of 1.83 m and a cross-sectional area of 2.4 m × 2.4 m. The fully transparent tunnel walls allow for clear visualization and laser-based measurements.

The fan unit is positioned at the entrance of the first section, providing airflow into the tunnel. The test model is mounted on a rigid metal stand by a bar crossing the center (30% chord) in the second section. The laser sheet, fan center, and wind tunnel center are precisely aligned along the central axis throughout the setup. It minimizes asymmetries in the airflow and improves PIV measurement accuracy by aligning the airflow as it passes through the test section.

The S809 airfoil, with a chord length of 0.3 m and a span of 0.1 m, is fabricated from aluminum and coated with black paint to minimize laser light reflection during PIV imaging. The blockage ratio for the experiment is 0.2% at 0° AOA, 0.16% at 6° AOA, and 0.28% at 20° AOA, indicating minimal interference from tunnel wall effects.

The experiments are conducted at a freestream velocity of 2.8 m/s, corresponding to a Reynolds number of 5.7×10^4, based on the airfoil chord length. The turbulence intensity is 10%, ensuring that the flow conditions represent the atmospheric boundary layer, where high turbulence is typically induced by the wake of upstream turbines. Figure 1 illustrates the wind tunnel setup, PIV system positioning, and airfoil installation.

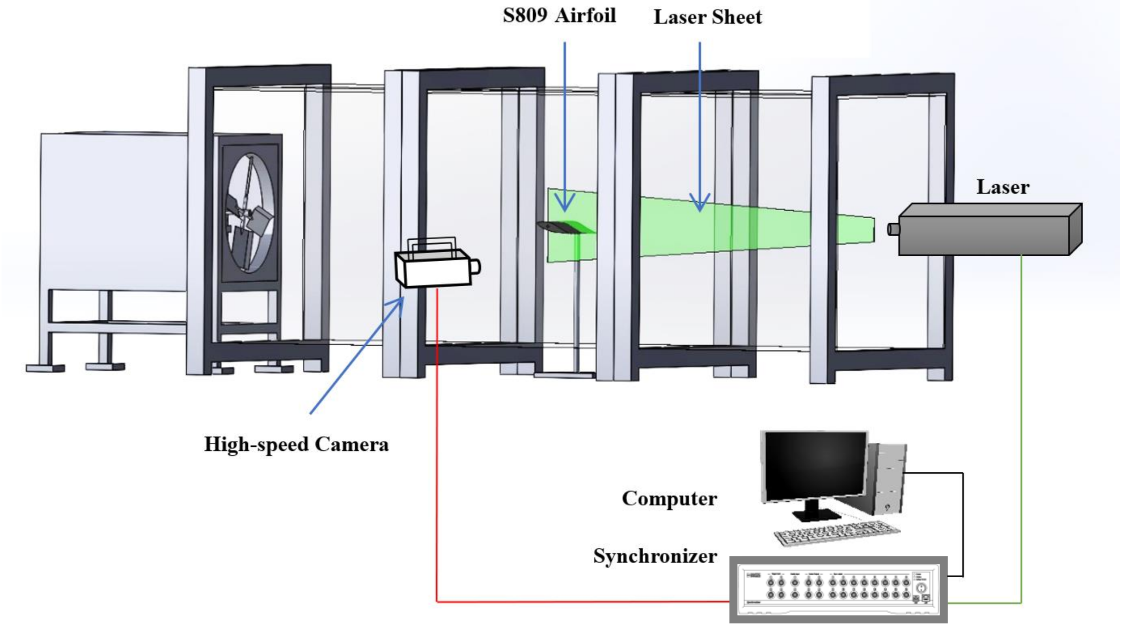

Figure 1. Experimental setup for PIV of airflow over an S809 airfoil (the laser sheet intersects with the airfoil mid-span).

As illustrated in Figure 1, the laser sheet is aligned along the mid-span of the airfoil to capture the flow field on its suction surface. Micrometer-sized glycerin oil droplets are introduced into the flow to enhance particle illumination in the measurement region. The PIV setup consists of a laser head, chiller, and high-speed camera. A double-pulse Nd: YLF laser, operating at a wavelength of 527 nm, generates pulses with an energy of 40 mJ. The pulse repetition rate is maintained at 200 Hz, determined by the freestream velocity. The laser sheet is oriented vertically with a thickness of approximately 1 mm in the measurement area.

A high-speed camera (Photron NOVA R3-4K) with a resolution of 4096 × 2304 pixels and a maximum frame rate of 750 frames per second is employed to capture images of the flow field. The effective measurement area covered by the camera is 66 cm × 37 cm. A 50 mm focal length lens with the f-number of 1.4 is positioned 121 cm from the laser sheet for a magnification of 0.16 mm/pixel. The camera axis is aligned perpendicular to the laser sheet to maintain optimal imaging geometry. The camera operates in double-frame mode, with an inter-frame time of 1 ms. The laser pulses and camera frames are synchronized using a synchronizer (model 9040U7122) with a precision of 1 ns, accurately capturing instantaneous velocity components. For each experiment, 500 instantaneous velocity images are recorded over 2.5 seconds.

The velocity vectors, including the streamwise (U) and normal (V) components, are processed using Dynamic Studio version 8.5. The software generates time-averaged flow fields and velocity contours for each case. Image pre-processing involves subtracting the minimum pixel intensity of each frame sequence to mitigate background noise, such as reflections from the stand and laser light, thereby enhancing particle visibility. Non-illuminated regions of the images are masked to reduce processing time.

As illustrated in Figure 2, laser illumination on the blade surface is limited beyond X/C = 0.16 at AOA = 0°; however, this limitation will be overcome in future studies by using an optical arm for the laser. The illuminated region extends to X/C = 0.05 for AOA = 6° and to X/C = -0.15 for AOA = 20°, after which no laser light reaches the surface. Velocity vector calculations are performed using adaptive interrogation areas, ranging from 32 × 32 pixels to 64 × 64 pixels, depending on particle density, with 50% and 75% overlap ratios, respectively. Post-processing includes vector validation, where outlier vectors are replaced with neighborhood-averaged values, and interpolation to address missing vectors, resulting in an 80% correct vector field per frame pair.

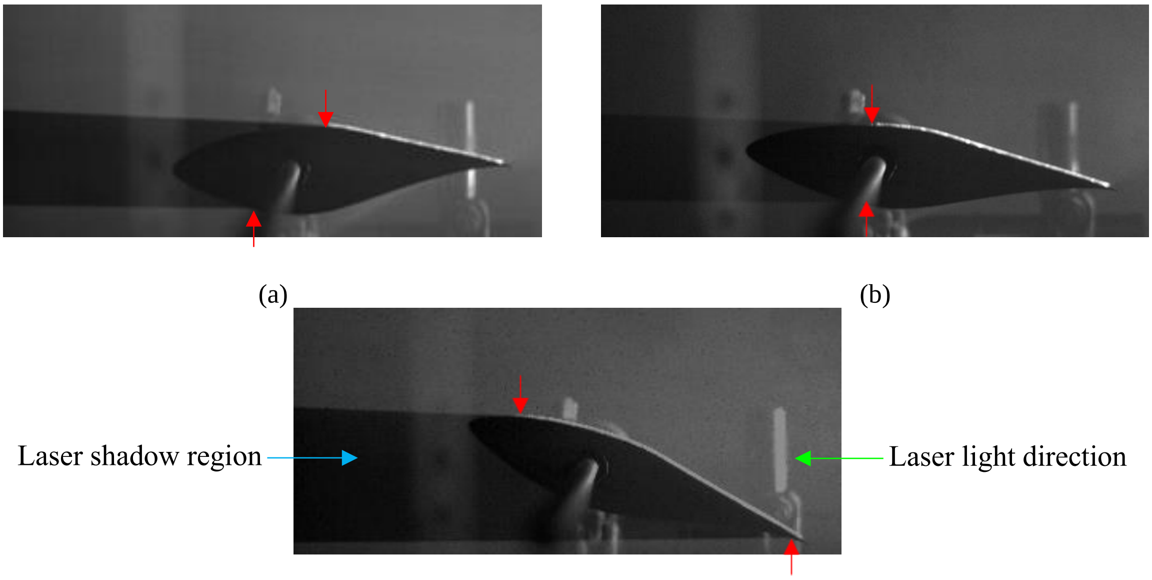

(a) (b)

(c)

Figure 2. Laser sheet position over S809 airfoil for (a) α = 0, (b) α = 6, and (c) α = 20, where the non-illuminated regions are marked by red arrows on both surfaces.

RESULTS AND DISCUSSION

The velocity magnitude contours for three different angles of attack, normalized by the free-stream velocity, are illustrated in Figure 3. The airfoil's center is defined at 30% of the chord, with the leading edge located at X/C = -0.3 and the trailing edge at X/C = 0.7. As previously mentioned, certain regions lack laser illumination due to the laser sheet position for each AOA, resulting in missing velocity measurements in those areas. This limitation affects the ability to capture the velocity field near the trailing edge in all cases.

As illustrated in Figure 3, the upstream flow remains mostly uniform in all experimental cases, indicating an undisturbed free stream with minimal fluctuations despite a high turbulence intensity. Along the airfoil surface, the velocity distribution is expected to exhibit attached flow at AOA = 0°. A low-velocity region is observed along the airfoil surface, corresponding to boundary layer development, where velocity gradually increases from zero at the surface due to the no-slip condition, eventually reaching the free-stream velocity. A transition from high to low velocity is evident on the suction surface. Near the leading edge and mid-chord regions, velocity increases due to decreased pressure, which causes the boundary layer to grow and become thicker. The velocity deficit region indicates the development of the wake, which is not perfectly symmetric since the S809 airfoil is cambered. This is expected for AOA = 0°, as the pressure distribution on the airfoil's upper and lower surfaces remains balanced, resulting in a symmetric wake and fully attached flow over the airfoil.

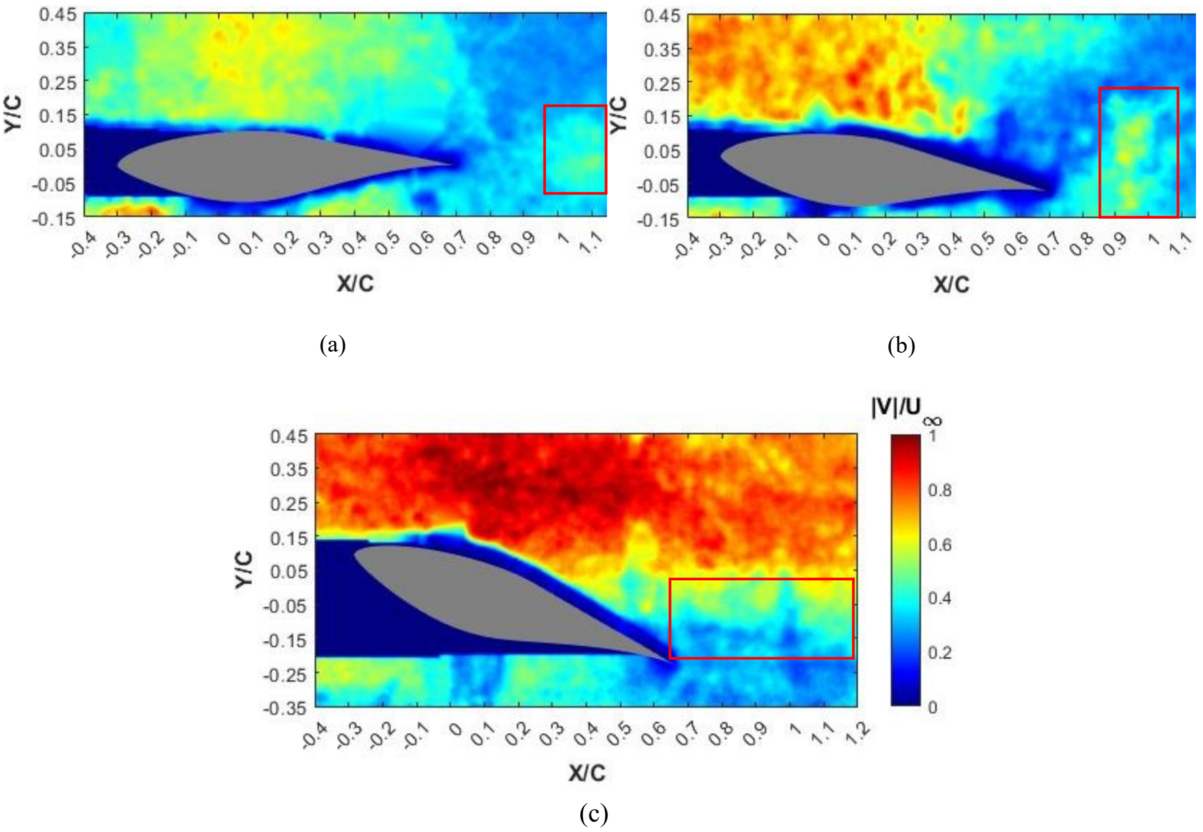

(a)

(b)

(c)

Figure 3. Normalized mean velocity magnitude for (a) α = 0, (b) α = 6, and (c) α = 20 (the dark areas are not illuminated by the laser and the wake is marked by the rectangle).

Figure 4 presents the normalized vertical velocity, where the absence of sudden variations for AOA = 0° suggests minimal lift generation under this condition. The flow remains mostly uniform, with minor fluctuations attributed to boundary layer growth and the turbulence level of the free stream flow. Hence, the velocity field is symmetric throughout the domain, with no signs of separation. However, slight variations in the wake region indicate boundary layer interactions. The vector field in Figure 6 further confirms these findings. The velocity vectors remain uniform and well-aligned in the free-stream region. The boundary layer is evident where vectors near the surface are reduced in magnitude. Additionally, the wake region appears narrow and symmetric, supporting the conclusion that no significant flow separation occurs at AOA = 0°.

By increasing AOA to 6° and 20°, lift generation also increases due to a higher pressure difference between the suction and pressure sides of the airfoil. Figure 3 shows that the velocity magnitude increases on the airfoil's upper surface, indicating flow acceleration due to the higher AOA. Conversely, the velocity on the lower surface is notably lower, corresponding to a high-pressure region that enhances energy production. Furthermore, the wake region becomes elongated and asymmetric, suggesting increased turbulence due to vortex shedding from the trailing edge.

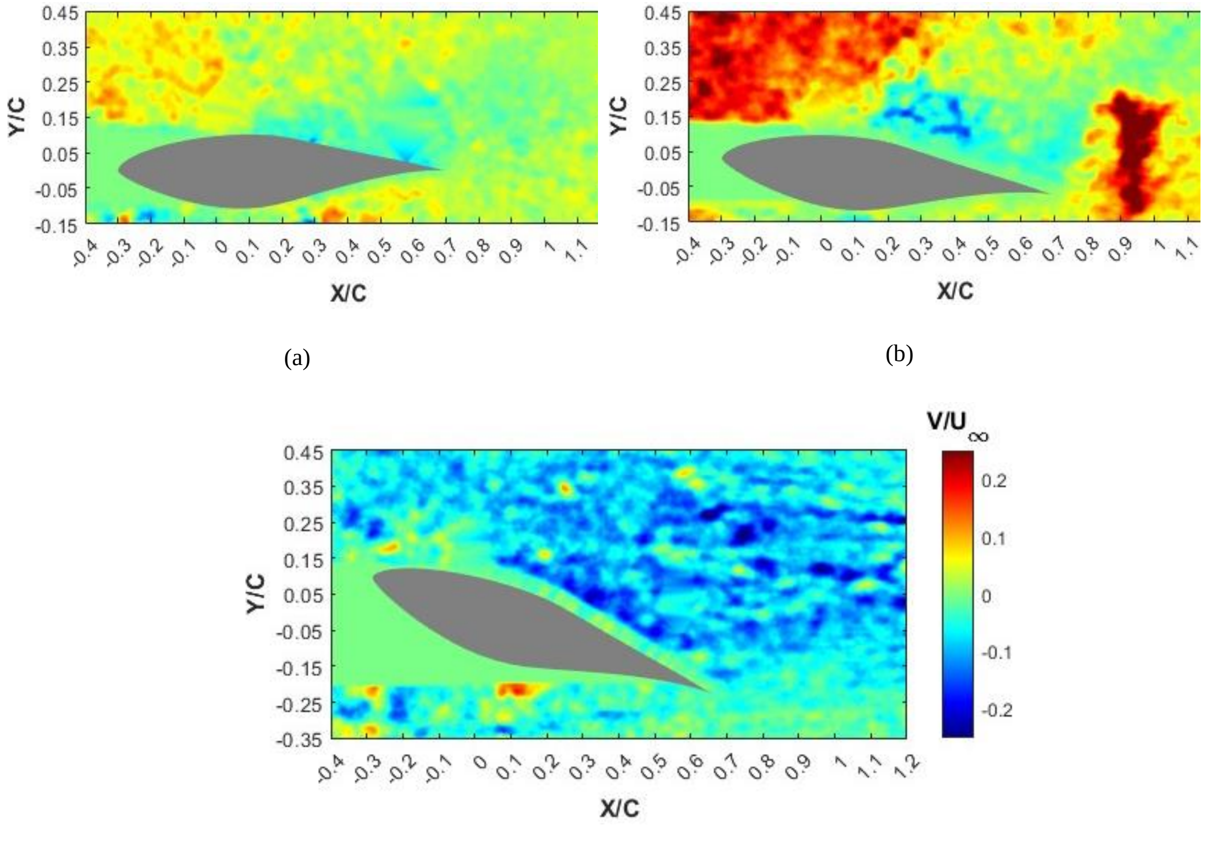

(a)

(b)

(c)

Figure 4. Normalized mean vertical velocity for (a) α = 0, (b) α = 6, and (c) α = 20 over airfoil (green areas near the airfoil surface lack laser illumination).

These findings align with the streamwise velocity contour shown in Figure 5, where an apparent velocity deficit is observed downstream. The wake region appears thickened and characterized by reduced momentum. Additionally, the upper portion of the wake displays significant velocity fluctuations, indicating strong mixing and turbulence. The streamwise velocity distribution highlights the separated flow region and distinctly separates the free-stream velocity region from the low-velocity zone.

Additionally, the normal velocity contours show that the airfoil curvature causes the flow to be deflected upward over the suction surface for the AOA = 6°. In the wake region, a significant change in the velocity component is observed, with a large area of positive vertical velocity, confirming the presence of vortex shedding downstream of the airfoil. The pronounced positive velocity region in the upper wake indicates that the influence of the suction surface extends well beyond the trailing edge.

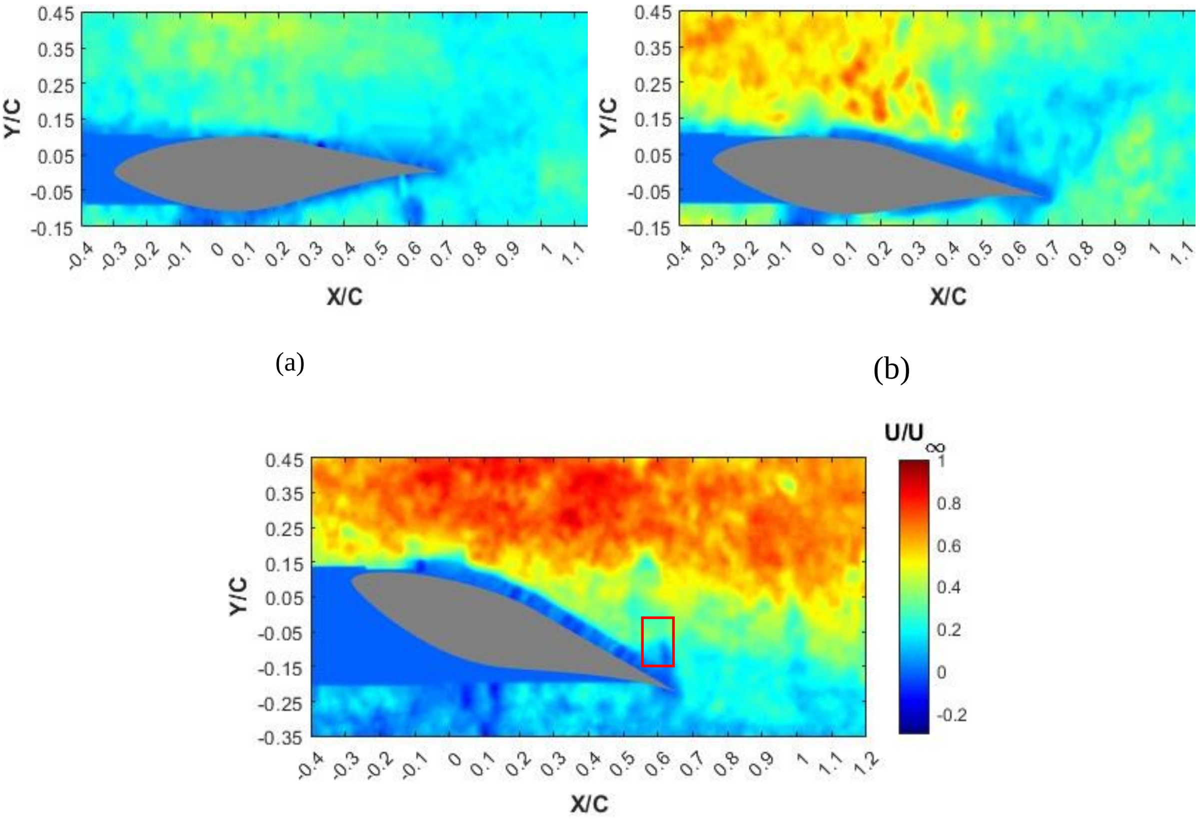

(a)

(b)

(c)

Figure 5. Normalized mean streamwise velocity for (a) α = 0, (b) α = 6, and (c) α = 20 over airfoil (the separation region is marked by a red rectangle in the third plot).

The vector fields in Figure 6 illustrate accelerating flow over the suction surface, where vectors become elongated, more streamlined, and follow the airfoil smoothly without signs of separation. Also, the incoming velocity vector field remains uniform and well-aligned, confirming that the test conditions are steady and undisturbed. However, in the wake region, the vector field becomes disrupted. A noticeable upward shift in the velocity component indicates an increase in turbulence fluctuations, indicating enhanced turbulence and the potential for flow separation as the airfoil sheds vortices downstream.

Increasing the AOA to 20° makes the onset of flow separation evident where the blade reaches stall. As shown in Figure 3, from the leading edge to approximately mid-chord (X/C = 0.4), the flow remains fast, as indicated by the predominantly dark red contour, suggesting that the boundary layer is still attached. Unlike lower AOA cases, where the flow smoothly transitions into the free stream, the velocity along the suction surface decreases significantly (cyan region) and extends further downstream, leading to a thickened boundary layer. Due to the adverse pressure gradient, the momentum slows down toward the trailing edge. Beyond X/C = 0.6, a sharp velocity drop is observed, indicating that the momentum is insufficient to keep the flow attached, resulting in flow separation.

Furthermore, the normalized vertical velocity contours reveal alternating positive (yellow areas) and negative (blue areas) velocity components in the wake region. This pattern suggests the presence of vertical fluctuations in the wake, likely caused by flow separation.

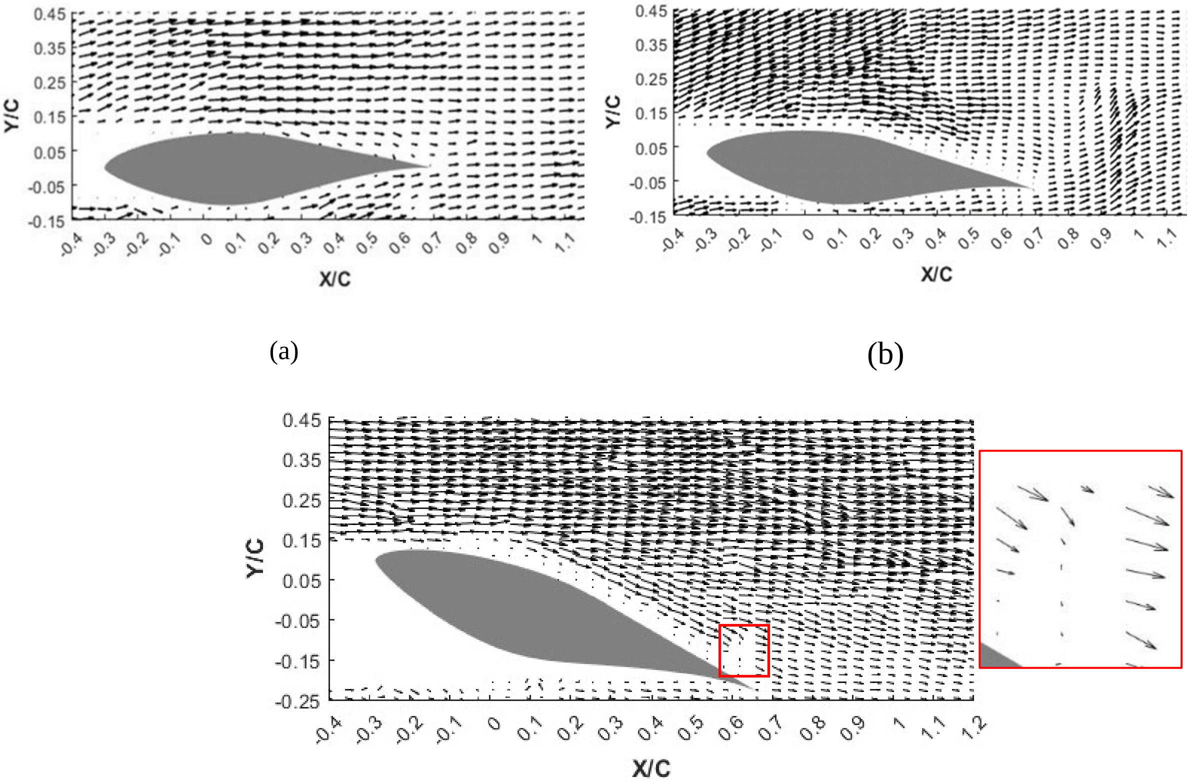

(a)

(b)

(c)

Figure 6. Mean velocity vector field for (a) α = 0, (b) α = 6, and (c) α = 20 over airfoil (the separation region is marked by a red rectangle in the third plot).

A more precise visualization of the separated region is evident in the vector field, where a noticeable deviation in vector direction occurs as the flow detaches from the airfoil surface. Compared to lower AOA cases, the vectors in the wake region appear more disorganized and disturbed, caused by increased turbulence. This chaotic motion in the wake results from vortex shedding, further emphasizing the instability and unsteadiness induced by flow separation.

Compared to a previous study by (Ma et al., 2010b) conducted at a Reynolds number similar to this experiment, where flow separation occurred closer to mid-chord, the present study demonstrates a delayed onset of separation. This difference can likely be attributed to the higher turbulence intensity in the current experiment. As discussed earlier, turbulence plays a crucial role in modifying boundary layer behavior. Since the boundary layer is very sensitive to the level of incoming turbulence, increasing it will delay the stall condition (Kamada et al., 2011).

Previous research has shown that increased turbulence intensity enhances the aerodynamic performance of airfoils by promoting higher lift generation across various AOA (Maldonado et al., 2015). A more energetic turbulent boundary layer, influenced by free-stream turbulence intensity, helps sustain momentum within the flow, delaying separation by overcoming the adverse pressure gradient. As a result, the flow remains attached to the suction surface for a longer distance along the chord, reducing early detachment and improving aerodynamic efficiency.

The velocity field distribution in this experiment provides insight into regions prone to ice accumulation on wind turbines operating in cold environments. At AOA = 0°, the attached flow and symmetric wake region result in a more uniform and evenly distributed rime ice formation. In contrast, as the AOA increases, the high-velocity region over the suction surface becomes more susceptible to droplet impingement due to the increased curvature of the airfoil. The separated flow region with strong vortex structures at higher AOA disperses droplets, leading to irregular ice formation. Moreover, the high turbulence intensity, which delays flow separation, can alter the location of ice growth and extend its spread downstream. These findings highlight the importance of studying flow behavior to develop effective de-icing systems and enhance wind turbine energy production in cold-weather regions.

CONCLUSIONS

The present study examined the velocity flow field patterns around the S809 airfoil by implementing the PIV technique at various AOAs. The findings illustrated that the boundary layer development is evident, which changes from zero at the surface to the free stream velocity. The velocity accelerates to the mid-chord region due to passing through the curvature of the airfoil and then decelerates due to an adverse pressure gradient. The velocity field is completely attached at low AOA, and the wake region is symmetric and narrow. By increasing the AOA, the wake region becomes wider as well as lifted upward, and more velocity fluctuation is obvious due to vortex shedding. However, by increasing the AOA to 20°, the separation occurs at X/C = 0.6, which is delayed as a result of high turbulence intensity in the experiment. Thus, the velocity decreases sharply in the separation region, while in the wake region, the velocity variation is more prominent, showing high turbulence energy. This powerful vortex structure can scatter droplets and, together with delay separation, can modify the ice covering area and thickness on the airfoil surface. By disturbing the droplet paths and enhancing mixing in the wake region, fewer droplets reach and adhere to critical areas of the airfoil. In addition, the downstream shift in separation point reduces the surface area exposed to low-energy flow conditions, which are more prone to droplet freezing and ice accumulation.

Additionally, the detailed velocity vector fields captured through PIV provide valuable insight into droplet trajectories and regions of small droplet impingement, offering a useful tool for ice prediction modeling. These findings have practical implications for the design of passive or active anti-icing strategies, especially for offshore wind turbines operating in severe atmospheric environments. Future work could incorporate experimental icing conditions or numerical simulations to further assess how high incoming flow turbulence influences ice accretion dynamics.

ACKNOWLEDGEMENTS

The authors gratefully acknowledge the financial support of the Natural Sciences and Engineering Research Council of Canada, Mitacs, and Waterford Energy Services Inc.

REFERENCES

Barber, S., Wang, Y., Jafari, S., Chokani, N. and Abhari, R.S. 2011. The impact of ice formation on wind turbine performance and aerodynamics. *Journal of Solar Energy Engineering, Transactions of the ASME* 133(1). doi: 10.1115/1.4003187.

Canada. National Energy Board. 2023. Available at: https://open.canada.ca/data/en/dataset/7643c948-d661-4d90-ab91-e9ac732fc737 [Accessed: 5 March 2025].

Han, Y., Palacios, J. and Schmitz, S. 2012. Scaled ice accretion experiments on a rotating wind turbine blade. *Journal of Wind Engineering and Industrial Aerodynamics* 109, pp. 55–67. doi: 10.1016/j.jweia.2012.06.001.

Ibrahim, G.M., Pope, K. and Naterer, G.F. 2023. Scaling formulation of multiphase flow and droplet trajectories with rime ice accretion on a rotating wind turbine blade. *Journal of Wind Engineering and Industrial Aerodynamics* 232. doi: 10.1016/j.jweia.2022.105247.

Kamada, Y., Maeda, T., Murata, J., Toki, T. and Tobuchi, A. 2011. Effects of Turbulence Intensity on Dynamic Characteristics of Wind Turbine Airfoil*. *Journal of Fluid Science and Technology* 6(3). doi: 10.1299/jfst.6.333.

Kelly, J., Vogel, C., Energy, R.W.-W. and 2022, undefined. 2021. Impact and mitigation of blade surface roughness effects on wind turbine performance. *Wiley Online LibraryJ Kelly, C Vogel, R WilldenWind Energy, 2022•Wiley Online Library* 25(4), pp. 660–677. Available at: https://onlinelibrary.wiley.com/doi/abs/10.1002/we.2691 [Accessed: 1 January 2025].

Ma, J., Xu, J., Guo, R. and Zhang, K. 2010a. PIV experimental study of a 2-D wind turbine airfoil under different Re number. *8th Annual International Energy Conversion Engineering Conference*. doi: 10.2514/6.2010-6513.

Ma, J., Xu, J., Guo, R. and Zhang, K. 2010b. *PIV Experimental Study of a 2-D Wind Turbine Airfoil under Different Re Number*.

Maldonado, V., Castillo, L., Thormann, A. and Meneveau, C. 2015. The role of free stream turbulence with large integral scale on the aerodynamic performance of an experimental low Reynolds number S809 wind turbine blade. *Journal of Wind Engineering and Industrial Aerodynamics* 142, pp. 246–257. doi: 10.1016/j.jweia.2015.03.010.

Parent, O. and Ilinca, A. 2011. Anti-icing and de-icing techniques for wind turbines: Critical review. *Cold Regions Science and Technology* 65(1), pp. 88–96. doi: 10.1016/j.coldregions.2010.01.005.

Wahidi, R., Lai, W., Hubner, J.P. and Lang, A. 2013. Time-averaged and time-resolved volumetric velocimetry measurements of a laminar separation bubble on an airfoil. *European Journal of Mechanics, B/Fluids* 41, pp. 46–59. doi: 10.1016/j.euromechflu.2013.04.003.

Wu, J., Xu, Q., Wu, F., Xia, Q., Xu, Q. and Li, S. 2023. Droplet Collection Efficiency Regularity of NACA0012 Airfoil Based on the Eulerian Method. *Aerospace* 10(5). doi: 10.3390/aerospace10050412.

Xie, Y., Chen, J., Qu, H., Xie, G., Zhang, D. and Moshfeghi, M. 2013. Numerical and Experimental Investigation on the Flow Separation Control of S809 Airfoil with Slot. *Mathematical Problems in Engineering* 2013(1), p. 301748. Available at: https://onlinelibrary.wiley.com/doi/full/10.1155/2013/301748 [Accessed: 5 January 2025].